Temporal subtraction of serial CT scans by large deformation diffeomorphic metric mapping (LDDMM) for identification of bone metastases

Technical Development

Advances in Knowledge: (up to 5 statements)

1. By using temporal subtraction (TS) images, the average reading time for detecting bone metastases on CT images decreased significantly from 384.3 to 286.8 seconds.
2. While statistically significant improvement in lesion detection could not be demonstrated, with subjective scores of 1-5, observers found that the TS images improved their diagnostic confidence from 3 to 4 in the median.

Implications for Patient Care: (up to 3 sentences)

For follow-up of cancer patients, our temporal subtraction technique can potentially facilitate more efficient detection of bone metastases on serial CT, although technical complexity and lack of wide availability remain a challenge for immediate applicability of our technique in routine clinical care of patients.

Summary statement:

TS images obtained from serial CT scans using non-rigid registration showed promise for

efficient detection of newly developed bone metastases.

Abstract

Purpose:

To determine the improvement of radiologists' efficiency and performance in detecting bone metastases on serial follow-up CT by a temporal subtraction (TS) technique based on an advanced non-rigid image registration algorithm.

Materials and Methods:

Our study was approved by our institutional review board, and informed consent was waived because this was a retrospective study. CT image pairs ("previous" and "current" scans of the torso) of 60 cancer patients (primary lesion: prostate, 14; breast, 16; lung, 20; liver, 10) were included, consisting of 30 positive cases with a total of 65 bone metastases depicted only on "current" images and confirmed by two radiologists who had access to additional imaging examinations and clinical courses, and 30 matched negative controls (no bone metastases). "Previous" CT images were semi-automatically registered to "current" CT images by the algorithm, and TS images were then created. Seven radiologists independently interpreted CT image pairs to identify newly developed bone metastases without and with TS images with at least 30 days interval. Jack-knife free-response receiver operating characteristics analysis was conducted to assess observer performance. Reading time was recorded, and usefulness was evaluated with subjective scores of 1-5, with 5 being extremely useful. Statistical significance of

these values was tested by the Wilcoxon signed-rank test.

Results:

The subtraction images depicted various types of bone metastases (osteolytic, 28; osteoblastic, 26; osteolytic-blastic mixed, 11) as temporal changes. The average reading time was significantly reduced from 384.3 to 286.8 seconds (Wilcoxon signed rank test, P=0.028). The average figure-of-merit value increased from 0.758 to 0.835; however, this difference was not significant (JAFROC analysis, P=0.092). The subjective usefulness survey response demonstrated a median score of 5/5 for use of the technique (range 3-5).

Conclusion:

TS images obtained from serial CT scans using non-rigid registration successfully depicted newly developed bone metastases and showed promise for their efficient detection.

Introduction

Early and accurate detection of bone metastases is one of the most important tasks in diagnostic imaging. If they are not treated appropriately, they can cause various complications, such as pathological fractures, as well as neural compression and pain, which could significantly deteriorate patients' quality of life.

For detecting bone metastases, Tc-99m bone scintigraphy has been recognized as one of the most effective methods for a long period, and ^{18}F-fluoro-2-deoxy-d-glucose positron emission tomography (^{18}F FDG-PET) has been shown to be useful by providing high sensitivity and specificity (1-4). Recently, 18F-Fluoride PET (^{18}F NaF-PET) has reported to have superior sensitivity to bone scintigraphy for the detection of bone metastases (5). Recent advancement in MR imaging also allows whole-body screening of bone metastases with fine image quality (6). However, those examinations are not always performed routinely for cancer patients.

Computed tomography (CT) has been used as the primary modality for a long time to examine local recurrence and distant metastases for clinical follow-up of cancer patients. Recent multi-detector CT has an ability to visualize faint lesions characterized by small osteolytic or

osteoblastic changes in trabeculae and/or bony cortex of bone metastases (7,8). While the capability of CT is improving continuously, with finer resolution and a better signal-to-noise ratio, the burden of detecting metastases on radiologists has been increasing, posing a significant challenge because of the huge amount of anatomical information. To improve radiologists' efficiency and performance in detecting bone metastases, we hypothesized that a temporal subtraction (TS) technique could enhance the detection of newly developed bone metastases on CT images. Detecting temporal changes is crucial in interpreting diagnostic images, and the benefit of detecting temporal changes using TS has been described in various fields (9-13); however, the application of TS for visualizing bone metastases on CT images has not been reported. The purpose of our study was to determine the usefulness of a TS technique based on an advanced non-rigid image registration algorithm called large deformation diffeomorphic metric mapping (LDDMM) for the detection of bone metastases on serial follow-up CT.

Materials and Methods

Our study was performed with a financial support based on a matching-fund project; Kyoto University/Canon joint research project named as Innovative Techno-Hub for Integrated Medical Bio-imaging of the Project for Developing Innovation Systems, with a support from Canon Inc., Anatomy Works, LLC. and the Ministry of Education, Culture, Sports, Science and Technology

(MEXT) of the Japanese Government. Authors in Kyoto University (R.S., M.Y., K.F., T.K., Y.E., T.A., K.T.) had control of inclusion of any data and information that might present a conflict of interest for authors (K.N., G.A., H.Y.: Canon Inc.; S.M., M.M.: Anatomy Works, LLC.). Our study was approved by our institutional review board; informed consent was waived because this was a retrospective study.

Subject Population

Images of two serial torso CT studies ("previous" and "current") of 60 cancer patients between 2007 and 2013 were selected in sequential from our clinical database, consisting of 30 positive cases with newly developed bone metastases only on the "current" study and 30 negative controls without any bone metastases. The inclusion criteria were: (1) known site of malignancy; (2) CT images of at least two time points were available; (3) one or more subsequent bone scintigraphy or FDG-PET/CT studies were available; and for positive cases, (4) the number of lesions was less than 10 per patient; (5) the minimum lesion diameter size was greater than 5 mm; and (6) the lesions were also suggestive of metastases on at least one of those studies (osteolytic and/or osteoblastic change on CT, and/or substantial focal uptake on FDG-PET or bone scintigraphy) and confirmed by continued growth on subsequent CT and/or clinical data supporting the diagnosis of bone metastases. The controls and their CT studies were selected to match the age, sex, primary lesion, and scan interval of the positive cases. These conditions were

confirmed, in consensus, by two radiologists (R.S., K.F.: 9 and 13 years of experience in interpretation of torso CT images, respectively) who did not participate in the observer study by consulting all available clinical information registered before and after the “current” study, including medical records, laboratory data, images, and reports of CT, bone scintigraphy and FDG-PET studies. A total of 65 bone metastases were identified in 30 cases and considered a reference standard. Scan area and use of intravenous contrast varied according to the patients’ diseases or status. The details of the cases and scan conditions, the range and average interval for the paired CT scans are summarized in Table 1.

Temporal Subtraction Method

Details of the process for creating TS images are described in the Appendix and Fig 1. In brief, “previous” CT images were manually registered to “current” ones to match the position of the bronchial bifurcation. The rest was performed automatically; affine transformation followed by the non-rigid registration algorithm called large deformation diffeomorphic metric mapping (LDDMM). TS images were obtained by subtracting the transformed “previous” images from “current” images.

Image Review

The location (humeral head-clavicle, sternum, scapula, rib, thoracic spine, lumbar spine, pelvis-femoral head) and severity of subtraction artifacts on TS images were recorded for each location to evaluate registration quality. Artifacts were graded using a three-point scale: 1, no artifact; 2, mild to moderate (partial band-like subtraction artifact in a bone); 3, severe (band-like subtraction artifact in a bone and/or apparent misalignment of a bone). The appearances of bone metastases (osteolytic, osteoblastic, or mixed) on TS images were recorded. This image review was performed by two radiologists (R.S., K.F.).

Observer Study

Seven radiologists (M.Y., T.K., Y.E. and T.A. and three other volunteers; range 6-28 years of experience in interpretation of torso CT images) independently interpreted a pair of “current” and “previous” CT images for each subject in axial stack mode. They were allowed to change window level and width. They were asked to identify new bone metastases by marking the location of each suspicious lesion with the percent likelihood of being metastasis. This experiment was a fully crossed multi reader multi case study and was performed using an in-house DICOM viewer (YAKAMI DICOM Tools Ver.1.4.5.0; http://www.kuhp.kyoto-u.ac.jp/~diag_rad/intro/tech/dicom_tools.html) (Fig 2). The image interpretation was conducted twice for the same cases, without first and then with TS images.

The order of cases in each reading session was randomized. At least 30 days of interval was set between two reading sessions to minimize the memory effect. In order to control practice effects, observers were trained to the viewer using six training cases before an actual observer study. The observers were informed of the patients' age, sex, and histology of the primary tumor while blinded to all other clinical data. They were asked to rate the confidence level of their interpretation for the entire study (Survey 1: 1, very low; 2, low; 3, moderate; 4, high; 5, very high) and the usefulness of TS images (Survey 2: 1, useless; 2, not very useful; 3, somewhat useful; 4, very useful; 5, extremely useful) using a five-point scale for each case. Reading time for identifying new bone metastases was also recorded. After all data were collected, those lesions affected beneficially or detrimentally by TS images were analyzed in terms of the location and its appearance. TS images were considered beneficial to lesions that at least one radiologist could detect only with TS images: specifically, lesions that were false-negative without TS images and true-positive with TS images under the condition that a likelihood of 51% or higher was considered positive. Conversely, TS images were considered detrimental to lesions that at least one radiologist could detect only without TS images: specifically, lesions that were true-positive without TS images and false-negative with TS images under the condition. Changes in sensitivity (Δsensitivity) between without and with TS images were also analyzed for each location and each appearance of bone metastases.

Statistical Analysis

The difference in age between the females and males of selected subjects was analyzed by Mann-Whitney's U test. Median scores for subtraction artifacts were compared among areas using the Kruskal-Wallis test followed by post hoc analysis using Mann-Whitney's U test with Bonferroni correction. Interobserver agreement was assessed by weighted kappa statistics. Sensitivity on lesion-based analysis, number of false-positives per case, sensitivity and specificity on case-based analysis, reading time and confidence level were compared between the two sessions using the Wilcoxon signed-rank test. Sensitivity and specificity were analyzed under the condition that a lesion with 51% or higher likelihood of being metastasis was considered positive. For a case-based analysis, a case with at least one positive lesion was considered positive. Jackknife free-response receiver operating characteristic (JAFROC) analysis (14, 15) was used to evaluate the radiologists' performance. The analysis was conducted using freely available JAFROC software (JAFROC, version 4; http://www.devchakraborty.com) with a random-readers and random-cases model. The Δsensitivity was compared among lesion location and appearance by the Kruskal-Wallis test. SPSS (IBM SPSS Statistics for Windows, Version 21.0. IBM Corp, Armonk, NY) was used for statistical analyses, and $P<.05$ was considered

significant.

Results

The processing time for LDDMM for each case ranged from approximately 2 to 10 hours depending on the scanning area. The average processing time for the images of the chest, chest-to-upper abdomen, and chest-to-pelvis were 2 hours and 32 minutes, 4 hours and 37 minutes, and 6 hours and 11 minutes, respectively. The age distribution in selected subjects was as follows: overall mean age, 66.5years ± 9.6, age range, 45-84 years; 32 men; mean age, 69.6 years ± 8.6 [standard deviation], age range, 52-84 years; 28 women, mean age, 63.0 years ± 9.5, age range, 45-81 years; p = 0.019. The details of identified bone metastases as reference standard were as follows: mean size, 20.5±14.0 mm; number of lesions per metastasis-positive patient, 2.2±1.3; number of lesions for each type of bone metastasis (osteolytic, 28; osteoblastic, 26; osteolytic-blastic mixed, 11).

The skeletal structure of “previous” and “current” CT images was almost perfectly registered except for the humeral head to clavicular area, scapulae, and ribs (Table 2). Obvious misalignments were observed more frequently in the scapulae than in other bones. In regard to the subtraction artifacts of ribs, almost all artifacts were noticed at the tips of ribs. In the bone

metastasis-positive cases, bone metastases were located in the clavicular-to-sternum area (n=7), scapulae (n=4), ribs (n=13), thoracic spines (n=8), lumbar spines (n=17), and pelvic bones (n=16). The appearance of bone metastases on TS images varied depending on the type of lesions. Osteolytic metastases were depicted as dark signals on TS images (Fig 3A). Osteoblastic changes were depicted as bright signals (Fig 3B). Mixed type metastases showed a heterogeneous appearance of dark and bright (Fig 3C). In some cases, non-neoplastic temporal bone changes, such as degenerative compression fracture, development of Schmorl's nodes, healed rib fractures, subchondral cysts and osteophytes, were also observed. Outside of the skeletal structure, artifacts were observed due to the difference in imaging conditions (e.g., with or without contrast agent) or large morphological changes in the gastrointestinal organs. Representative cases with these changes or subtraction artifacts are shown in Fig 4.

The average sensitivity on lesion-based analysis was not significantly increased from 58.0% (37.7 / 65) to 65.9% (42.9 / 65) using TS images. The average number of false-positives per case was not significantly increased from 0.19 to 0.23 (P=0.344). The average sensitivity and specificity on case-based analysis were not significantly increased from 78.0% (23.4 / 30) and 92.9% (27.9 / 30) to 80.0% (24.0 / 30) and 96.7% (29.0 / 30) (P=0.443 and P=0.066), respectively. The free-response receiver operating characteristic (FROC) is shown in Fig 5. The

figure-of-merit (FOM) value (equivalent value of the area under the receiver operating characteristic curve) for each radiologist was improved for all except one, and the average FOM value was improved from 0.758 to 0.835; however, this was not significant (P=0.092).

The average reading time was decreased significantly from 384.3 seconds to 286.8 seconds (P=0.028). The radiologists' confidence in their interpretation (Survey 1) improved significantly from 3 to 4 (P=0.043) in the median using TS images. Usefulness of TS images (Survey 2) gave sufficiently high scores (5 in the median), and all observers recognized the advantage of TS images (3 at minimum). The FOM, reading time, and results of the two surveys are shown in Table 3.

The review of the results showed both beneficial and detrimental effects of TS images (Fig 6). Beneficial effects were seen in 39 lesions; one lesion was beneficially affected for six radiologists, and six lesions were for four radiologists. In these cases, bone metastases appeared as small osteolytic lesions without apparent destruction of the bony cortex. These lesions were found at ribs, pelvic bones, and the posterior column of the vertebrae. Detrimental effects were seen in 33 lesions; four lesions were detrimentally affected for three radiologists, and no lesion was for more than three radiologists. Three of them were located on or close to the scapulae,

where severe subtraction artifacts were often observed. Both beneficial and detrimental effects were seen in 20 lesions. Examples of these cases, demonstrating the advantage and disadvantage of TS images, are shown on Fig 6.

The appearance-wise and lesion-wise comparisons of Δsensitivity showed no significant differences; however, there was a decrease in sensitivity at the scapulae with TS images in this analysis (Table 4).

Discussion

Image registration methods are particularly important in radiotherapy and volumetric imaging (16-18). One of the major applications is TS; however, this technique has not yet been put into practical use in clinical CT images even for the skeletal structure, although it consists of rigid bones. This could be attributable to the substantial differences in bone configurations between serial CT scans due to different patient positioning or degree of inspiration, requiring highly elastic and accurate image transformation for registration. To reduce the misregistration artifacts and enhance the diagnostic value of TS, accurate image registration is inevitable. LDDMM is a well-known non-rigid registration algorithm that is designed to cope with a large amount of deformation. It has been previously confirmed that LDDMM is feasible for serial chest CT

images (19). Thus, this method was adopted for creating precise TS images in our study. The result showed sufficient registration for skeletal structures on serial CT images to visualize the various appearances of bone metastases successfully. Although its incremental value was not significant, our technique showed promise for improving radiologists' performance in detecting bone metastases. It was also shown that the improvement did not depend on lesion appearance. Previous TS studies reported that TS is more beneficial for residents who have less experience in diagnostic imaging than attending radiologists (10,11). Since all observers in our study were highly trained radiologists, an investigation with residents remains as future work. In addition, under the present experimental conditions, the observers were given unlimited time for the detection of bone metastases. Consequently, they tended to take longer time in reading CT images compared to their routine clinical work. Therefore, investigating the advantage of TS images in the actual clinical setting in a prospective study is also important.

In our study, the TS images helped detect small lytic lesions located at the ribs or pelvic bones. Several computer-aided detection methods for bone metastases on torso CT have been reported previously (20-22); however, they focused only on vertebral lesions. Although vertebrae are the most vulnerable sites for bone metastases (23), metastases can occur at any site in the skeletal bones. Our TS method was capable of visualizing bone metastases in all scanned areas, which is

highly advantageous compared to these methods. In some cases, we used image sets of “previous” and “current” CT studies with different conditions of contrast enhancement since scanning conditions in serial CT are not always the same in clinical setting. The difference may harm the registration accuracy of bones and cause subtraction artifacts in enhanced organs or vessels. These issues require further verification. However, the harm would be minute to none due to higher density of bones than organs even if enhanced. The artifacts would not substantially hinder radiologists’ detecting bone metastases because the artifacts are distributed outside bones, on which radiologists focus their attention during the detection. However, our method was not sufficiently successful in visualizing bone metastases located on or close to the scapulae (Δsensitivity = -0.18) due to subtraction artifacts, since the position of the scapulae can vary largely for each scan. Further improvement of registration accuracy for such problematic regions is, thus, an important future research target.

When radiologists use a computer-aided diagnosis (CAD) system, viewing and assessing its output may require additional time (19). However, our TS technique even improved the efficiency of this task of detecting newly developed bone metastasis by significantly decreasing reading time (25% reduction) for this task. The result of the survey also showed increased diagnostic confidence. These results could be understood because less confidence in the

diagnosis would lead to repetitive image viewing time.

Our TS images visualized not only temporal changes caused by bone metastases, but also various non-neoplastic changes, such as degenerative and traumatic changes. Although this seems to confuse radiologists, the result showed sufficiently high average specificity for the detection of metastases. This might be because TS is based on a simple principle, in contrast with CAD, which typically uses complex image features.

There were several limitations in our study. First, the bone lesions were not confirmed by histology**.** In the clinical setting, it is very rare to perform a biopsy to obtain histological confirmation of bone metastases when a primary lesion is evident. Therefore, the best effort was made by consulting all available clinical information as mentioned in “Subject Population” section. Second, this method requires large computational resources and long calculation times because of the large data size of high-resolution CT images, and no comparison was made to any other registration algorithm on the aspect of computational effort and registration accuracy. Optimizing the registration algorithm or considering more efficient algorithm will be an important future work before introducing this system into the clinical workflow. Third, the LDDMM algorithm was applied solely to serial clinical CT scans without simulations using

phantoms. The empirical setting we previously used showed satisfactory results; however, more detailed optimization based on numerical simulations may lead more precise registration and these would be one of the future tasks. Fourth, we have not investigated the effect of variability in imaging conditions, such as use of contrast agent and selection of scanning protocol, on TS images of bones. Fifth, we evaluated the utility of TS images only for detecting newly developed bone metastases. In a previous study, we used a Jacobian map, which indicates local volume change, to visualize temporal changes in existing lesions (19). It could be that a Jacobian map of bone metastasis could reflect temporal changes in the volume or shape of existing lesions. Sixth, since our ultimate goal is to apply this TS technique to cancer patients with various disease stages including those who have bone metastases in the initial assessment, our study population may differ from those cancer population (selection bias). Seventh, all observers read the cases without first and then with TS images. We consider that the reading-order bias could be kept minimal by setting reading interval for a washout period; however, the reading-order bias might not be eliminated completely.

In conclusion, TS images obtained from serial CT scans using non-rigid registration successfully depicted newly developed bone metastases and showed promise for their efficient detection.

ACKNOWLEDGEMENTS

This work is partly supported by the Innovative Techno-Hub for Integrated Medical Bio-imaging of the Project for Developing Innovation Systems, from the Ministry of Education, Culture, Sports, Science and Technology (MEXT). The supercomputer of ACCMS, Kyoto University, was used in this research work. Authors S.M. and M.M. own “AnatomyWorks”, and S.M. is its CEO. This arrangement is being managed by the Johns Hopkins University in accordance with its conflict of interest policies.

References

1. Bury T, Barreto A, Daenen F, Barthelemy N, Ghaye B, Rigo P. Fluorine-18 deoxyglucose positron emission tomography for the detection of bone metastases in patients with non-small cell lung cancer. Eur J Nucl Med. 1998;25(9):1244-1247.

62 Hahn S, Heusner T, Kummel S, et al. Comparison of FDG-PET/CT and bone scintigraphy for detection of bone metastases in breast cancer. Acta Radiol. 2011;52(9):1009-1014.

3. Cook GJ, Houston S, Rubens R, Maisey MN, Fogelman I. Detection of bone metastases in breast cancer by 18FDG PET: differing metabolic activity in osteoblastic and osteolytic lesions. J Clin Oncol. 1998;16(10):3375-3379.

4. Ng SH, Chan SC, Yen TC, et al. Staging of untreated nasopharyngeal carcinoma with PET/CT: comparison with conventional imaging work-up. Eur J Nucl Med Mol Imaging. 2009;36(1):12-22.

5. Damle NA, Bal C, Bandopadhyaya GP, Kumar L, Kumar P, Malhotra A, Lata S. The role of 18F-fluoride PET-CT in the detection of bone metastases in patients with breast, lung and prostate carcinoma: a comparison with FDG PET/CT and 99mTc-MDP bone scan. Jpn J Radiol. 2013 Apr; 31(4):262-9.

6. Pasoglou V, Michoux N, Peeters F, et al. Whole-body 3D T1-weighted MR imaging in

patients with prostate cancer: feasibility and evaluation in screening for metastatic disease. Radiology. 2015 Apr;275(1):155-66.

7. Groves AM, Beadsmoore CJ, Cheow HK, et al. Can 16-detector multislice CT exclude skeletal lesions during tumour staging? Implications for the cancer patient. Eur Radiol. 2006;16(5):1066-1073.

8. Kalogeropoulou C, Karachaliou A, Zampakis P. Radiologic evaluation of skeletal metastases: role of plain radiographs and computed tomography. In: Kardamakis D, Vassilious V, ed. Bone Metastases. 1st ed. Berlin, Germany. Springer, 2009: 119-136.

9. Ishida T, Ashizawa K, Engelmann R, Katsuragawa S, MacMahon H, Doi K. Application of temporal subtraction for detection of interval changes on chest radiographs: improvement of subtraction images using automated initial image matching. J Digital Imaging. 1999;12(2):77-86.

10. Abe H, Ishida T, Shiraishi J, et al. Effect of temporal subtraction images on radiologists' detection of lung cancer on CT: Results of the observer performance study with use of film computed tomography images 1. Academic Radiology. 2004;11(12):1337-1343.

11. Aoki T, Murakami S, Kim H, et al. Temporal subtraction method for lung nodule detection on successive thoracic CT soft-copy images. Radiology 2013;271(1):255-261.

12. Beigelman-Aubry C, Raffy P, Yang W, Castellino RA, Grenier PA. Computer-aided detection of solid lung nodules on follow-up MDCT screening: evaluation of detection, tracking,

and reading time. AJR Am J Roentgenol. 2007;189(4):948-955.

13. Shiraishi J, Appelbaum D, Pu Y, Li Q, Pesce L, Doi K. Usefulness of temporal subtraction images for identification of interval changes in successive whole-body bone scans: JAFROC analysis of radiologists' performance. Academic Radiology. 2007;14(8):959-966.

14. Dorfman DD, Berbaum KS, Metz CE. Receiver operating characteristic rating analysis: Generalization to the population of readers and patients with the Jackknife method. Investigative Radiology. 1992;27(9):723-731.

15. Chakraborty DP, Berbaum KS. Observer studies involving detection and localization: modeling, analysis, and validation. Medical Physics. 2004;31(8):2313-2330.

16. Cao K, Ding K, Amelon RE, Du K, Reinhardt JM, Raghavan ML, Christensen GE. Intensity-based registration for lung motion estimation. In: Ehrhardt J, Lorenz C. 4D Modeling and estimation of respiratory motion for radiation therapy, 1st ed. Berlin, Germany. Springer, 2013; 125-158

17. Hodneland E, Hanson EA, Lundervold A, Modersitzki J, Eikefjord E, Munthe-Kaas AZ. Segmentation-driven image registration-application to 4D DCE-MRI recordings of the moving kidneys. Image Processing, IEEE Transactions on. 2014;23(5):2392-2404.

18. Wu G, Wang Q, Lian J, Shen D. Reconstruction of 4D-CT from a single free-breathing 3D-CT by spatial-temporal image registration. Inf Process Med Imaging. 2011;22():686-698.

19. Sakamoto R, Mori S, Miller MI, Okada T, Togashi K. Detection of time-varying structures by large deformation diffeomorphic metric mapping to aid reading of high-resolution CT images of the lung. PloS One. 2014;9(1):e85580.

20. O'Connor SD, Yao J, Summers RM. Lytic Metastases in Thoracolumbar Spine: Computer-aided Detection at CT—Preliminary Study 1. Radiology. 2007;242(3):811-6.

21. Burns JE, Yao J, Wiese TS, Muñoz HE, Jones EC, Summers RM. Automated detection of sclerotic metastases in the thoracolumbar spine at CT. Radiology. 2013;268(1):69-78.

22. Hammon M, Dankerl P, Tsymbal A, et al. Automatic detection of lytic and blastic thoracolumbar spine metastases on computed tomography. European radiology. 2013;23(7):1862-70.

23. Kakhki VR, Anvari K, Sadeghi R, Mahmoudian AS, Torabian-Kakhki M. Pattern and distribution of bone metastases in common malignant tumors. Nucl Med Rev Cent East Eur. 2013;16(2):66-9.

Table 1:

Characteristics of the subjects for the observer study

	Age, y (range)	Sex		Primary lesion				Average interval of scans, month (range)	Scan coverage		Scan condition ("previous"/"current")			
		Male	Female	Breast	Lung	Liver	Prostate		Chest-pelvis	Chest-upper abdomen	Chest	CE/CE	nCE/CE or CE/nCE	nCE/nCE
BM-negative	66.0±10.6 (45-84)	16	14	8	10	4	8	14.5±8.8 (2-42)	16	5	9	10	3	17
BM-positive	67.1±8.9 (49-83)	16	14	8	10	6	6	16.0±11.1 (2-41)	15	7	8	13	12	5
Total	66.5±10.6 (45-84)	32	28	16	20	10	14	15.2±9.9 (2-42)	31	12	17	23	15	22

BM: bone metastasis, CE: contrast-enhanced, nCE: non-contrast-enhanced

Table 2:

Median score of subtraction artifact in each location

	Humeral head-clavicle	Sternum	Scapula	Rib	Thoracic spine	Lumbar spine	Pelvis-femoral head
Median score	2*	1	3*	2*	1	1	1
κ	0.92	1.00	0.88	0.59	1.00	0.78	0.89

Note. The subtraction artifact was graded by a three-point scale: 1, no artifact; 2, mild to moderate (partial band-like subtraction artifact in a bone); and 3, severe (band-like subtraction artifact in a bone and/or apparent misalignment of a bone).

*: significantly high compared to the spine and pelvic areas on post hoc analysis ($P<0.001$)

Table 3:

FOM values, reading times, and results of surveys for seven radiologists

	FOM		Reading time [sec] (average)		Survey 1 (median)		Survey 2 (median)
Reader	Without TS	With TS	Without TS	With TS	Without TS	With TS	
1	0.863	0.880	494	354	3	4	5
2	0.745	0.860	237	191	3	3	4
3	0.746	0.800	395	343	4	4	5
4	0.761	0.755	151	108	3	4	4
5	0.618	0.890	308	346	3	3	3
6	0.755	0.837	659	424	3	4	5
7	0.818	0.819	446	241	3	4	5
overall	0.758	0.835	384	287*	3	4	5

Note. Survey 1: Please indicate your confidence level for the diagnosis on a 5-point scale (1, very low; 2, low; 3, moderate; 4, high; 5, very high).
Survey 2: Is the temporal subtraction image useful? Please answer based on a 5-point scale (1, useless; 2, not very useful; 3, somewhat useful; 4, very useful; 5, extremely useful).
* shows significant difference.

Table 4:

Appearance-wise and lesion-wise comparisons of Δsensitivity for detecting bone metastases.

Note. A positive observation was defined as a likelihood score of 51% or higher assigned by an observer.

	Appearance			Location						
	Osteolytic (n=28)	Osteoblastic (n=26)	Mixed (n=11)	Humeral head-clavicle (n=1)	Sternum (n=6)	Scapula (n=4)	Rib (n=13)	Thoracic spine (n=8)	Lumbar spine (n=17)	Pelvis-femoral head (n=16)
Average Δsensitivity	0.10	0.07	0.01	0.57	0.00	-0.18	0.12	0.14	0.07	0.05

Figure legends

Fig 1:

Flowchart of our temporal subtraction (TS) method for skeletal bones.

Fig 2:

Screen-shots of the image viewer for the observer study. The image stacks in the upper row show "previous" (A) and "current" (B) CT images (age 67, male, lung cancer). TS images are shown in the left column of the lower row (C). When an observer clicks on a suspicious lesion, the dialog for rating the likelihood (low to high) of being bone metastasis appears (D).

Fig 3:

Bone metastases on TS images. TS images visualize bone metastases with various appearances and locations as temporal changes (arrow) (I_p, "previous" CT images; I_c, "current" CT images; I_s, TS images). Osteolytic, osteoblastic, and osteolytic-blastic mixed metastases are depicted as a dark signal (A - age 71, male lung cancer), a bright signal (B - age 61, male, lung cancer) and a heterogeneous dark and bright signal (C - age 66, female, lung cancer), respectively.

Fig 4:

Subtraction artifacts and benign changes on TS images. Obvious misalignments are frequently observed at the humeral head and/or scapula (A - age 64, female, breast cancer). The tips of the ribs often show band-like mild subtraction artifacts (B - age 66, female, breast cancer, arrow). Non-neoplastic temporal bone changes such as degeneration or traumatic changes (C - age 76, female, lung cancer, degenerative compression fracture on a thoracic spine; D - age 71, male, lung cancer, arrow, traumatic sclerotic change on a rib), and artifacts due to the differences in imaging conditions (A, subtraction of non-contrast-enhanced images from contrast enhanced images) are also observed.

Fig 5:

Average FROC curves without and with TS images. The radiologists' performance increases using TS images, but this difference is not significant (P=0.092).

Fig 6:

Bone metastases that can and cannot be detected with TS images. TS images are especially

beneficial for detecting small osteolytic lesions or metastases with no apparent destruction of the cortex (A - age 82, male, hepatocellular carcinoma, B - age 69, male, prostate cancer). Bone metastases located on the scapulae (C - age 64, female, breast cancer, D – age 66, female, breast cancer) are less easily detected on TS images.

FN: false-negative, TP: true-positive.

Fig 1: Flowchart of our temporal subtraction (TS) method for skeletal bones.

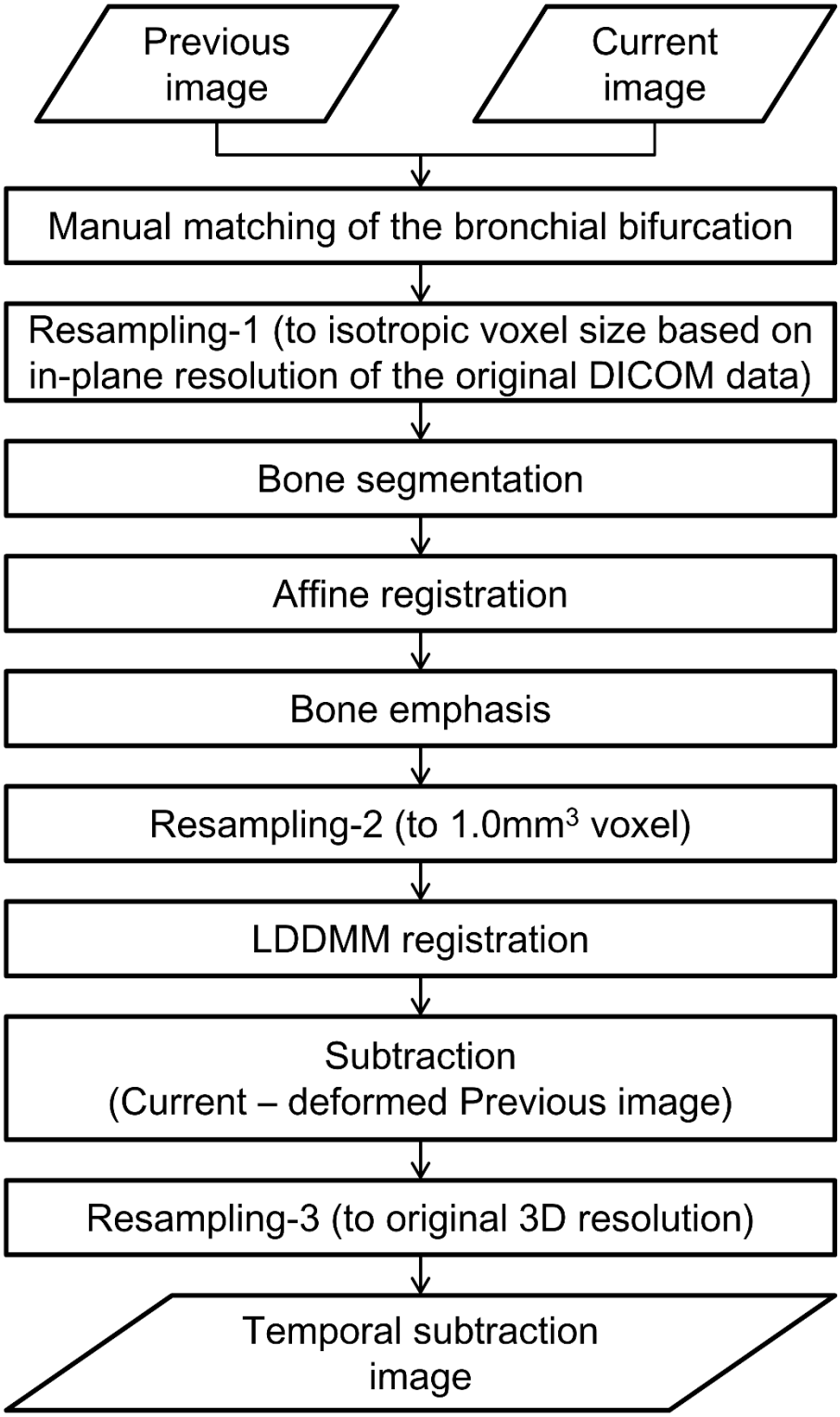

Fig 2: Screen-shots of the image viewer for the observer study. The image stacks in the upper row show “previous” (A) and “current” (B) CT images (age 67, male, lung cancer). TS images are shown in the left column of the lower row (C). When an observer clicks on a suspicious lesion, the dialog for rating the likelihood (low to high) of being bone metastasis appears (D).

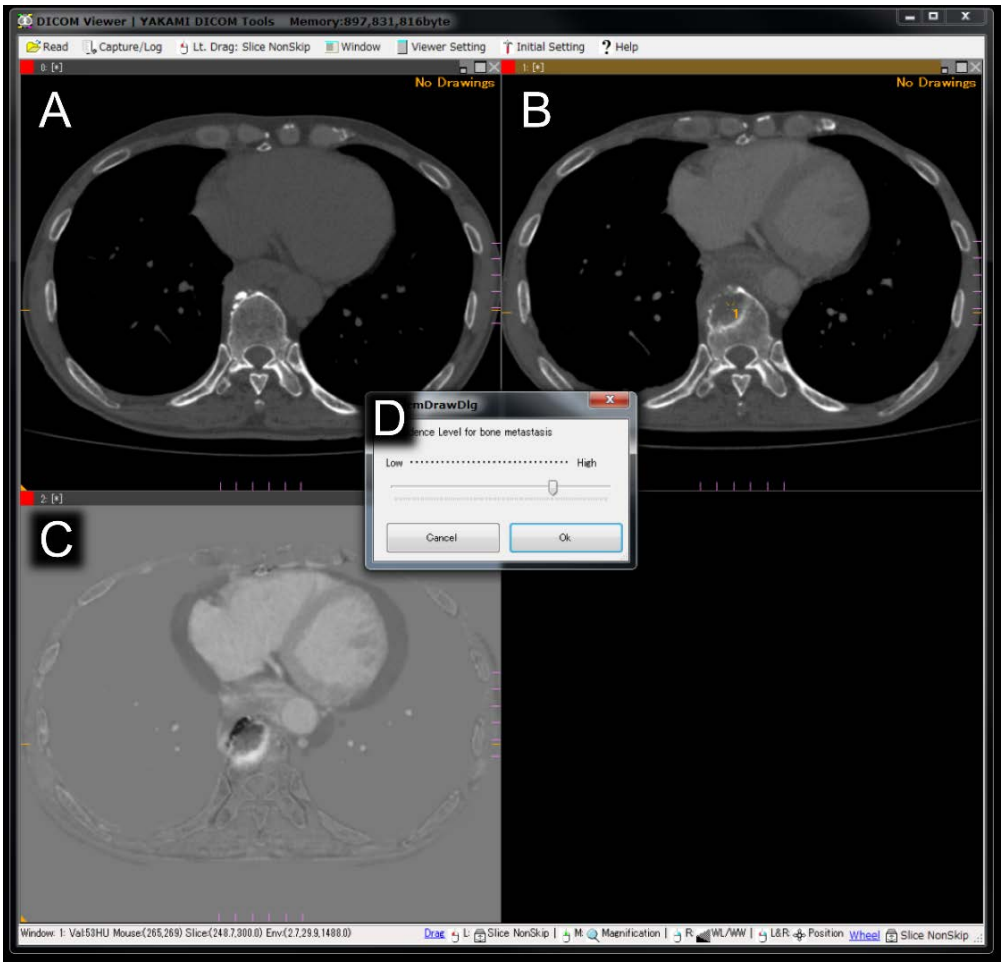

Fig 3: Bone metastases on TS images. TS images visualize bone metastases with various appearances and locations as temporal changes (arrow) (I_p, "previous" CT images; I_c, "current" CT images; I_s, TS images). Osteolytic, osteoblastic, and osteolytic-blastic mixed metastases are depicted as a dark signal (A - age 71, male lung cancer), a bright signal (B - age 61, male, lung cancer) and a heterogeneous dark and bright signal (C - age 66, female, lung cancer), respectively.

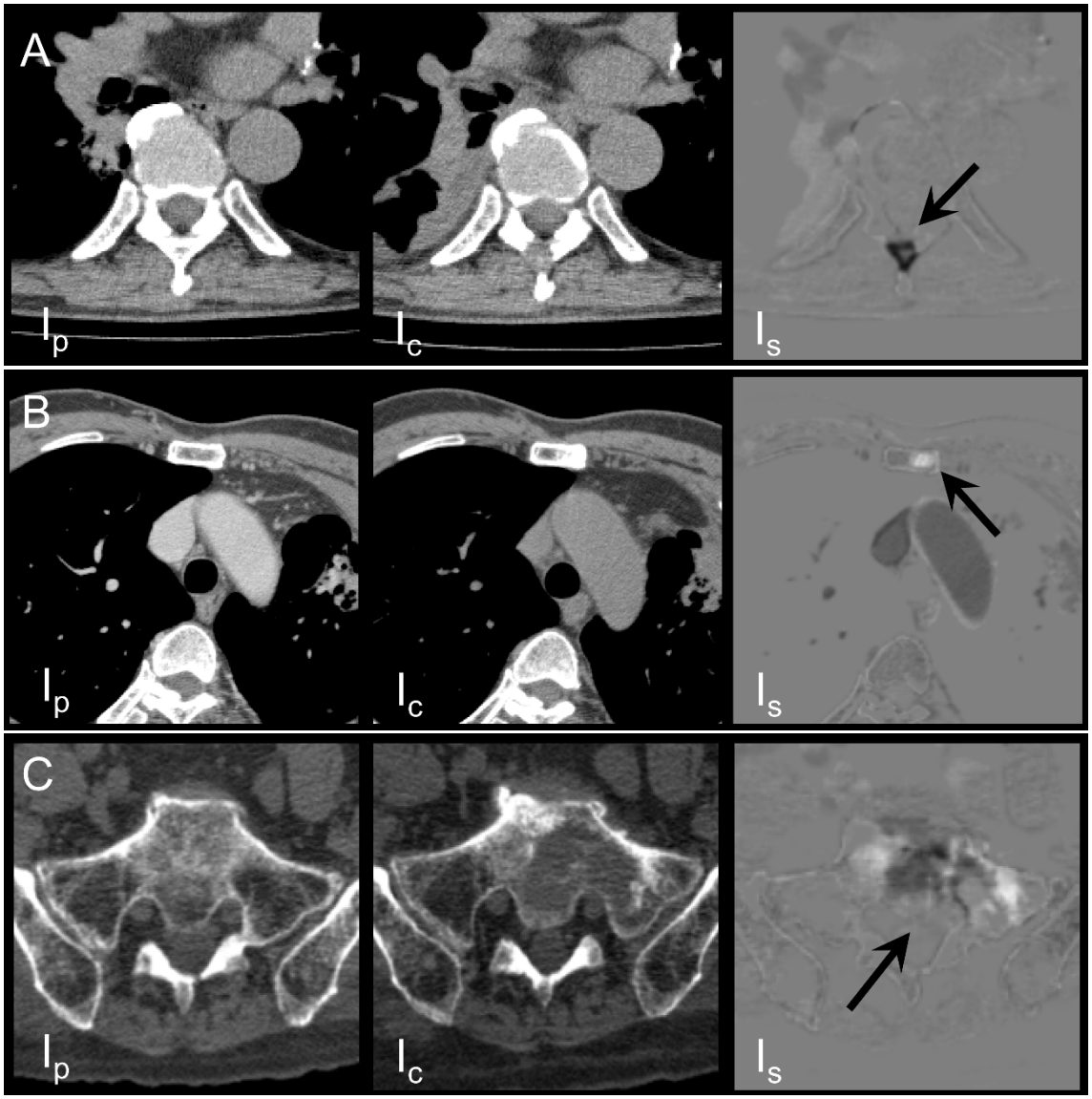

Fig 4: Subtraction artifacts and benign changes on TS images. Obvious misalignments are frequently observed at the humeral head and/or scapula (A - age 64, female, breast cancer). The tips of the ribs often show band-like mild subtraction artifacts (B - age 66, female, breast cancer, arrow). Non-neoplastic temporal bone changes such as degeneration or traumatic changes (C - age 76, female, lung cancer, degenerative compression fracture on a thoracic spine; D - age 71, male, lung cancer, arrow, traumatic sclerotic change on a rib), and artifacts due to the differences in imaging conditions (A, subtraction of non-contrast-enhanced images from contrast enhanced images) are also observed.

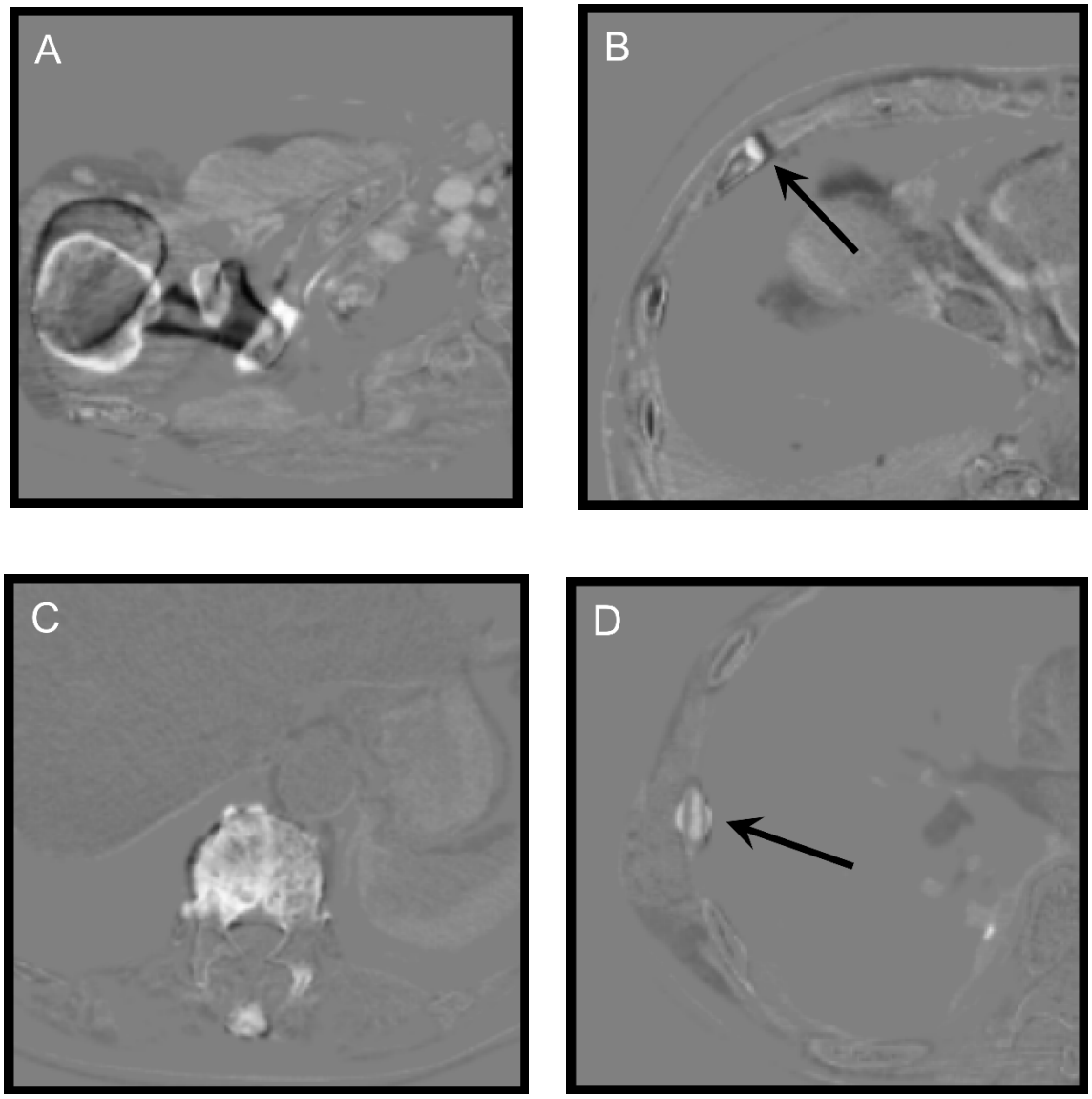

Fig 5:

Average FROC curves without and with TS images. The radiologists' performance increases using TS images, but this difference is not significant (P=0.092).

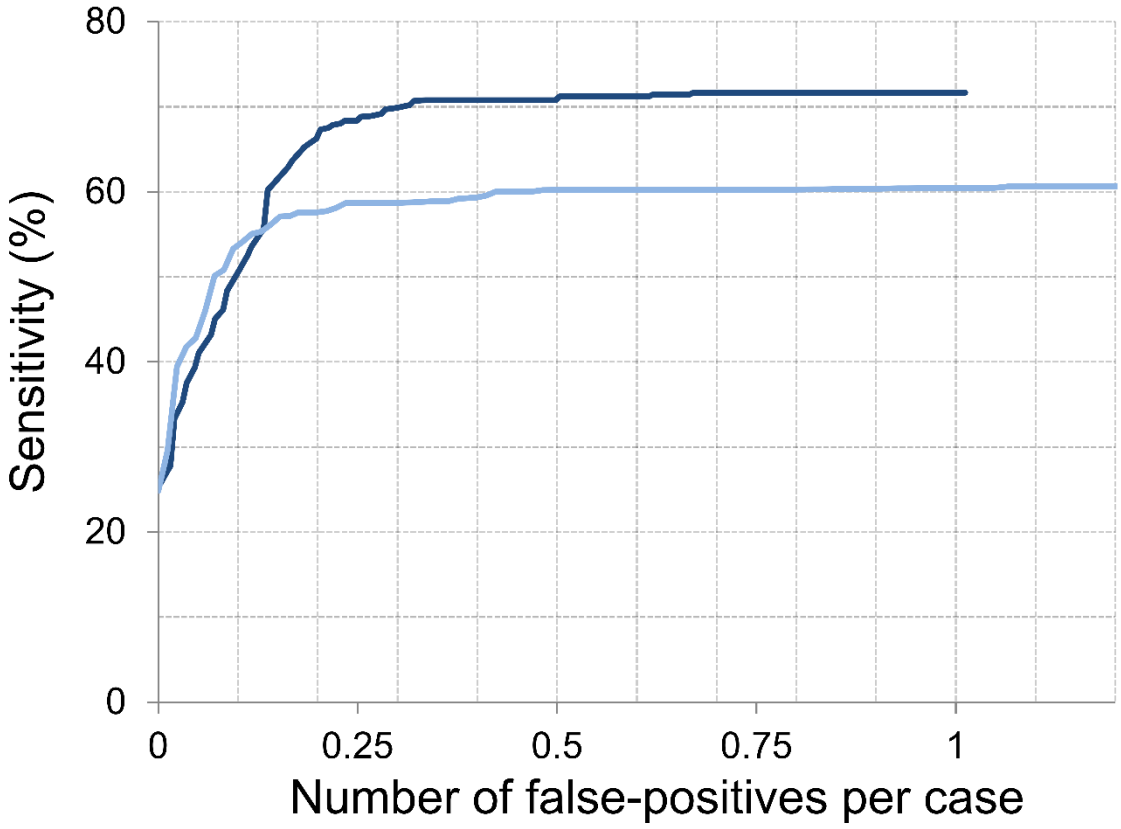

Fig 6: Bone metastases that can and cannot be detected with TS images. TS images are especially beneficial for detecting small osteolytic lesions or metastases with no apparent destruction of the cortex (A - age 82, male, hepatocellular carcinoma, B - age 69, male, prostate cancer). Bone metastases located on the scapulae (C - age 64, female, breast cancer, D – age 66, female, breast cancer) are less easily detected on TS images.
FN: false-negative, TP: true-positive.

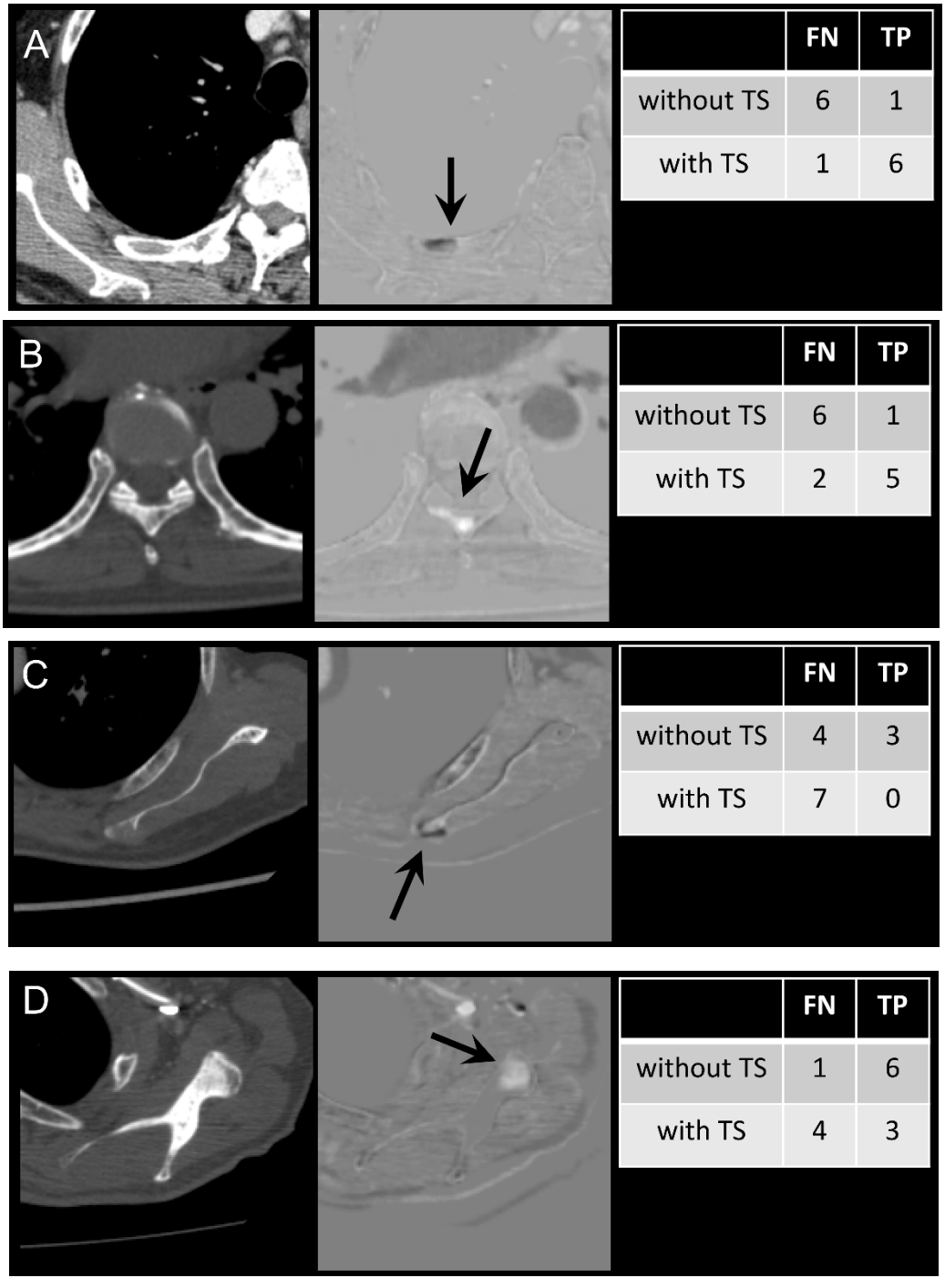

	FN	TP
without TS	6	1
with TS	1	6

	FN	TP
without TS	6	1
with TS	2	5

	FN	TP
without TS	4	3
with TS	7	0

	FN	TP
without TS	1	6
with TS	4	3

Appendix

Temporal Subtraction Method

TS images were created by subtracting the semi-automatically transformed previous images from the current images. Fig.1 presents a flowchart of the temporal subtraction system, and more detailed version of the flowchart is also shown in Fig.7. Here, all image processing were done in the three dimensional space. The process was as follows.

Step.1 Preparation:

"Previous" CT images were manually initialized to match the position of the bronchial bifurcation on "current" CT images by an engineer, who is one of the authors (K.N.). Then, CT images of both time points were resampled to isotropic voxels based on the in-plane resolution of the original DICOM data, which is 0.685mm (Fig.8 (a)).

Step.2 Bone area segmentation (and body area segmentation):

An objective of this step was to extract the bone area from CT images of both time points. First, median filtering (mask size: 3×3×3) was performed to reduce noises in CT images. Second, body area segmentation was performed based on a thresholding (-200 Hounsfield units (HU)) with morphological operations (opening and closing, radius = 1 voxel) and a hole filling process. This segmentation result of body area was used as a processing mask in the following bone

segmentation process. Moreover, for the sake of saving processing times in later steps, a bounding box which fits to this body area was automatically calculated for each previous and current image, and it was used to crop both CT image and a bone segmentation result. Third, a binary mask image that corresponded to the cortical bone area was extracted with a threshold value of 250 (HU) (Fig.8 (b)). Finally, the extracted bone area was refined by morphological closing process (radius = 20 voxel) in order to fill in holes (Fig.8 (c)).

Step3. Affine registration:

"Previous" images were globally registered to "current" images by affine transformation. The transformation matrix was calculated by using bone area segmentation results of the previous and current images from step 2. Regarding image size of the two images, the size of the previous image was matched to the size of the current image during this transformation process.

Step4. Bone emphasis and Resampling:

A bone window setting (window level=200 HU, window width=400 HU) was applied to each resampled CT image (Fig.8 (d)). These bone-emphasized "current" and transformed "previous" images were resampled to 1-mm isotropic voxels to reduce the data size because our next step requires much computational efforts.

Step5. LDDMM registration:

Those images from step 4 were further registered by using an algorithm called LDDMM [1,

2]. LDDMM is one of the non-rigid image registration algorithm originated from Pattern Theory [3], which is specifically designed for a large amount of deformation. It computes a diffeomorphic transformation between two images, while preserving the topology of the object. Therefore, it has been studied over past decades for applications in the area known as "Computational Anatomy" [4]. Past studies have shown its strength in fields such as MRI neuroscience and biomedical engineering [5, 6, 7]. However, its utilization and application to the registration of the bone structures has not yet been reported.

To deal with large displacement between two time-point images, LDDMM was performed using cascading processing, in which the elasticity of transformation was gradually increased [6, 7]. Since the average registration error of LDDMM for serial lung CT images was sufficiently low (less than 1 mm) in a previous study [7], the same setting was used in our study.

Step 6. Subtraction and Resampling to original image resolution:

TS images were obtained by subtracting the transformed “previous” images from the “current” images. Note that this process was done using bone emphasized images. Therefore, the subtraction was not calculated in Hounsfield unit. Finally, TS images were then upsampled to match the original resolution of “current” CT images.

All CT images were acquired with the same multi-detector CT scanner (Aquilion 64;

Toshiba Medical Systems, Otawara, Japan). Auto Exposure Control (AEC) was used in image acquisitions, and a soft-tissue kernel was used as a reconstruction kernel in all images. Settings of tube voltage were set as 120 kVp in 117 images and 135 kVp in 3 images (three pairs of the images had inconsistent tube voltage setting). CT images were reconstructed with a field of view of 350 mm in a 512 by 512 matrix (0.685 by 0.685 mm in-plane resolution) and a 1.0-mm slice thickness. Average processing times and ranges of image data size for each process of the flow chart are summarized in table 5 and 6. All processing except for LDDMM registration step were conducted with a desktop computer (Intel(R) Core(TM) i7-3930K CPU 3.20GHz, 32.0GB memory). For LDDMM, all image processing was conducted with the supercomputer of the Academic Center for Computing and Media Studies (ACCMS), Kyoto University (Appro 2548X; Processor, Intel Xeon E5; Clock, 2.6 GHz; number of cores, 16; memory, 150 GB). Parallelized computing was implemented, and the amount of memory usage was approximately 60 GB depending on the size of the input reference image. The LDDMM algorithm was developed at the Center for Imaging Sciences at Johns Hopkins University [2], and it was installed on the ACCMS as a part of a joint research project. All these image processing were implemented as a pipeline by one of the authors (K.N.), and it is a proprietary software designed for our study.

APPENDIX REFERENCES

[1]. Beg MF, Miller MI, Trouvé A, Younes L. Computing large deformation metric mappings via geodesic flows of diffeomorphisms. Int J Comput Vision. 2005;61(2):139-157.

[2] Software at CIS: lddmm-volume: Namespace; Center for Image Science, Johns Hopkins University; http://cis.jhu.edu/software/lddmm-volume/namespace.php. Updated May, 30, 2013. Accessed November 4, 2016.

[3]. Grenander U, Miller MI. Pattern Theory From Representation to Inference, Oxford University Press. 2007; 468-493.

[4]. Miller MI, Qiu A. The emerging discipline of Computational Functional Anatomy. Neuroimage. 2009; 45(1): S16–S39.

[5]. Ceritoglu C, Tang X, Chow M, et al. Computational analysis of LDDMM for brain mapping. Front Neurosci. 2013; 7: 151.

[6]. Ceritoglu C, Oishi K, Li X, et al. Multi-contrast large deformation diffeomorphic metric mapping for diffusion tensor imaging. Neuroimage. 2009;47(2):618-627.

[7]. Sakamoto R, Mori S, Miller MI, Okada T, Togashi K. Detection of time-varying structures by large deformation diffeomorphic metric mapping to aid reading of high-resolution CT images of the lung. PloS One. 2014;9(1):e85580.

Table 5:

Average processing time [hr:mm:sec]

	chest	chest to upper abdomen	chest to pelvis
Resampling-1	0:00:01	0:00:02	0:00:03
Bone segmentation	0:03:33	0:04:49	0:07:14
Affine registration	0:00:38	0:01:26	0:01:38
Bone emphasis	0:00:01	0:00:02	0:00:02
Resampling-2	0:00:03	0:00:03	0:00:05
LDDMM registration	2:32:24	4:37:27	6:10:50
Subtraction	< 0:00:01	< 0:00:01	< 0:00:01
Resampling-3	0:00:11	0:00:14	0:00:18

Table 6:

Range of input image data size in three dimensions

		chest	chest to upper abdomen	chest to pelvis
Resampling-1	x size	[512]	[512]	[512]
	y size	[512]	[512]	[512]
	z size	[294, 394]	[377, 552]	[589, 750]
Bone segmentation	x size	[512]	[512]	[512]
	y size	[512]	[512]	[512]
	z size	[428, 575]	[563, 806]	[859, 1097]
Affine registration / Bone emphasis	x size	[496, 512]	[511, 512]	[507, 512]
	y size	[263, 415]	[292, 417]	[271, 408]
	z size	[428, 575]	[563, 806]	[859, 1097]
Resampling-2	x size	[512]	[511, 512]	[507, 512]
	y size	[263, 415]	[292, 417]	[271, 403]
	z size	[428, 575]	[563, 806]	[859, 1097]
LDDMM registration / Subtraction / Resampling-3	x size	[350]	[320, 380]	[320, 380]
	y size	[180, 284]	[208, 284]	[186, 298]
	z size	[292, 392]	[376, 550]	[586, 748]

Figure legends

Fig. 7

Detailed flowchart of our temporal subtraction (TS) method.

Fig. 8

Examples of image process results of our temporal subtraction system (A - CT image after "resampling-1", B - extracted bone area after thresholding, C - extracted bone area after morphological refinement, D - bone emphasized image).

Fig. 7: Detailed flowchart of our temporal subtraction (TS) method.

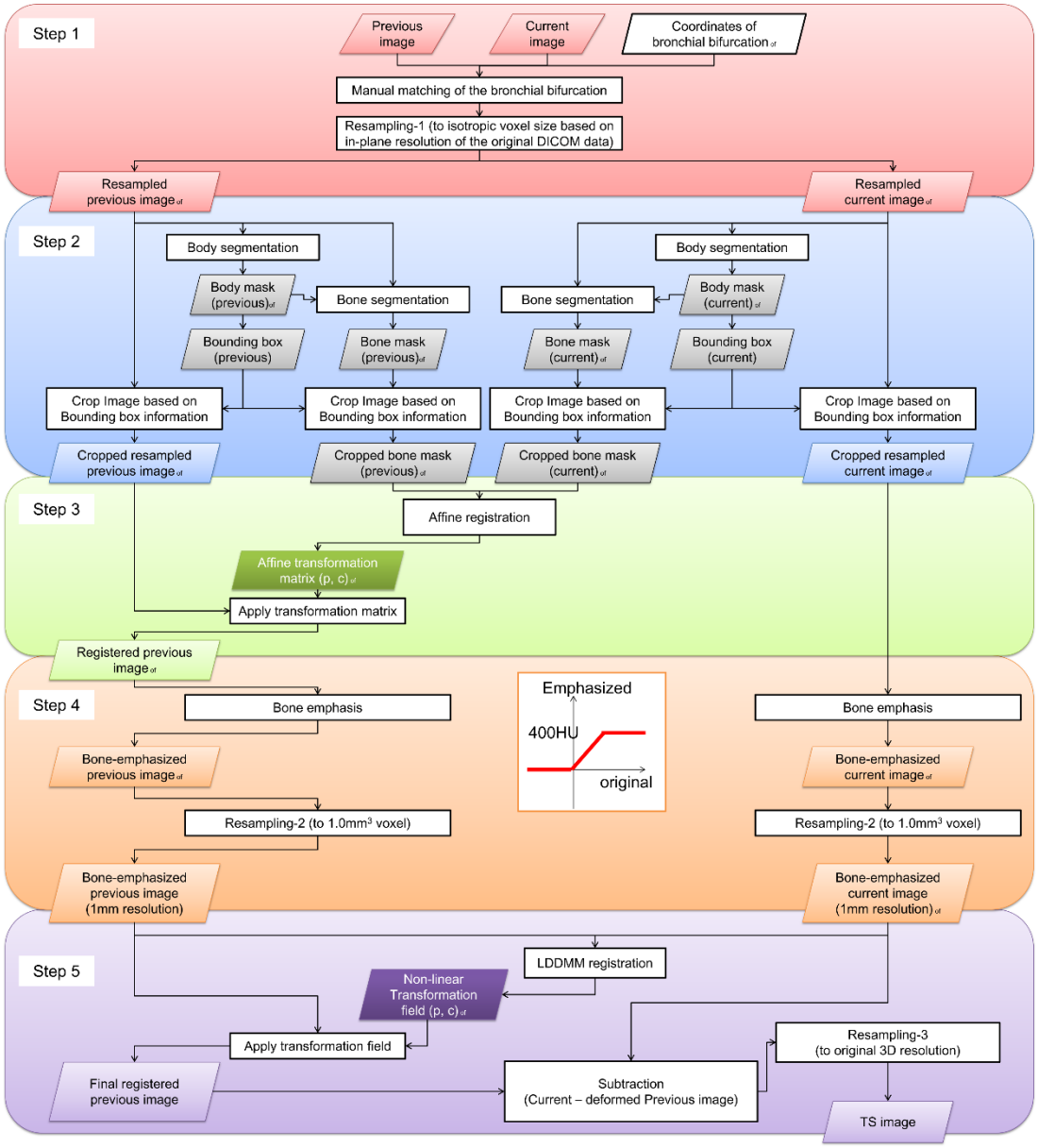

Fig. 8: Examples of image process results of our temporal subtraction system (A - CT image after "resampling-1", B - extracted bone area after thresholding, C - extracted bone area after morphological refinement, D - bone emphasized image).

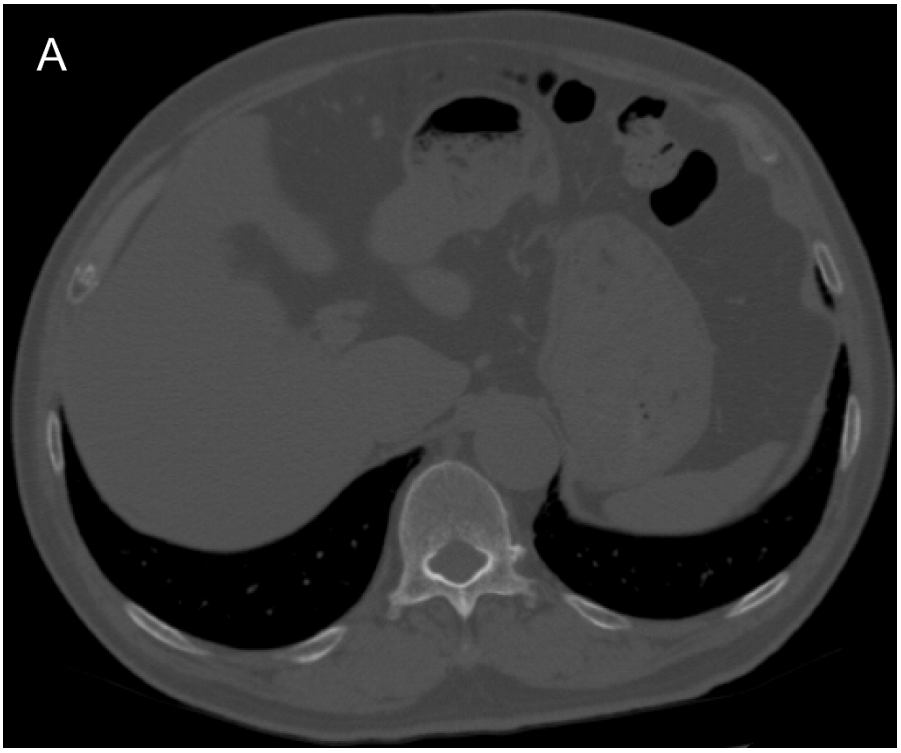

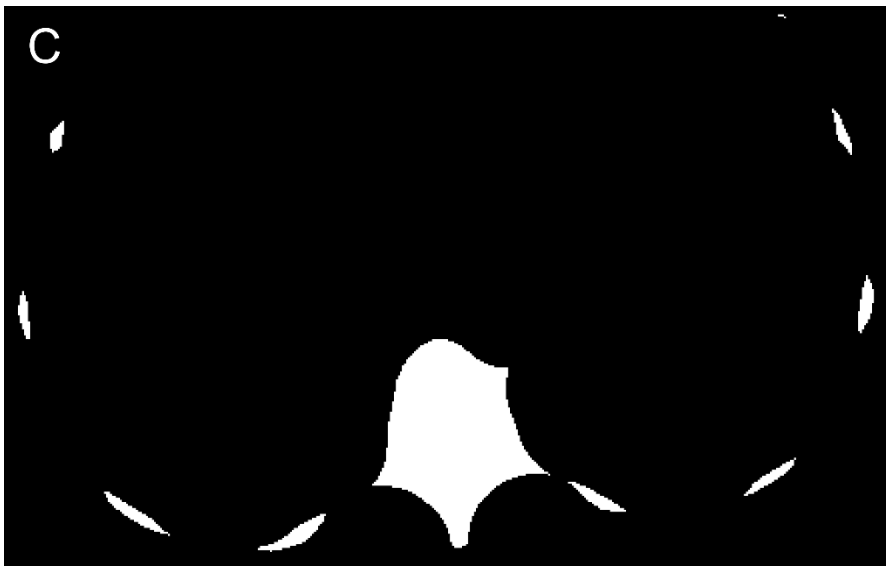
C

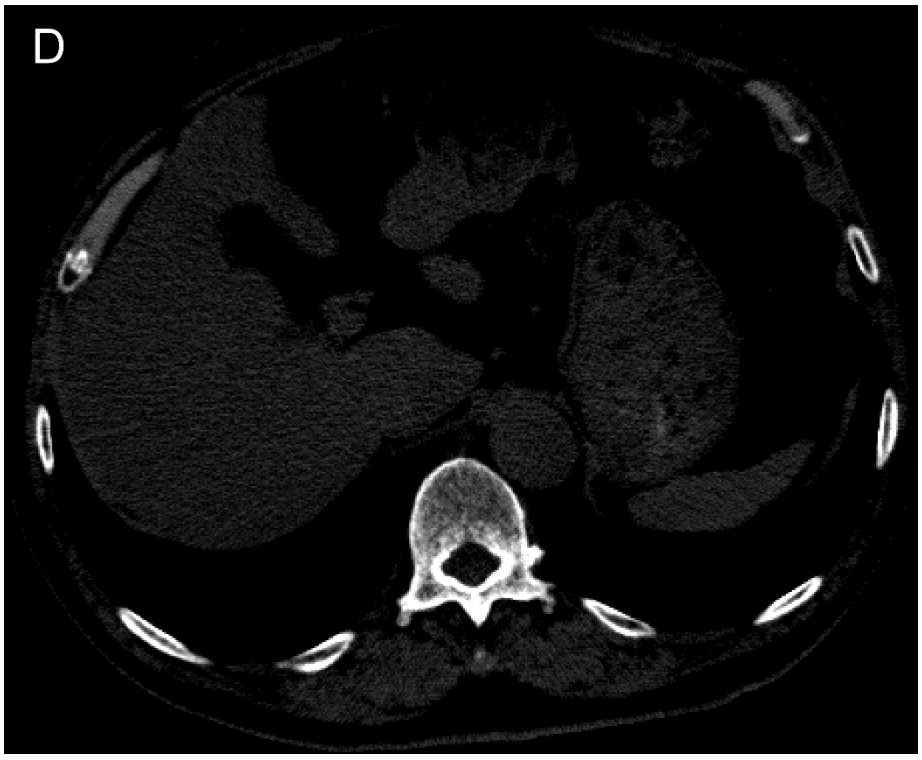
D